A New Mechanism for Mode Water Formation Involving Cabbeling and Frontogenetic Strain at Thermohaline Fronts. Part II: Numerical Simulations

CALLUM J. SHAKESPEARE

Research School of Earth Sciences, and ARC Centre of Excellence in Climate System Science, Australian National University, Canberra, Australian Capital Territory, Australia

LEIF N. THOMAS

Department of Environmental Earth System Science, Stanford University, Stanford, California

(Manuscript received 2 January 2017, in final form 20 April 2017)

ABSTRACT

Submesoscale-resolving numerical simulations are used to investigate a mechanism for sustained mode water formation via cabbeling at thermohaline fronts subject to a confluent strain flow. The simulations serve to further elucidate the mechanism and refine the predictions of the analytical model of Thomas and Shakespeare. Unlike other proposed mechanisms involving air–sea fluxes, the cabbeling mechanism, in addition to driving significant mode water formation, uniquely determines the thermohaline properties of the mode water given knowledge of the source water masses on either side of the front. The process of mode water formation in the simulations is as follows: Confluent flow associated with idealized mesoscale eddies forces water horizontally toward the front. The frontogenetic circulation draws this water near adiabatically from the full depth of the thermohaline front up to the surface 25 m, where resolved submesoscale instabilities drive intense mixing across the thermohaline front, creating the mode water. The mode water is denser than the surrounding stratified fluid and sinks to fill its neutral buoyancy layer at depth. This layer gradually expands up to the surface, and eddies composed entirely of this mode water detach from the front and accumulate in the diffluent regions of the domain. The process continues until the source water masses are exhausted. The temperature–salinity (T–S) relation of the resulting mode water is biased to the properties of the source water that has the larger isopycnal T–S anomaly. This mechanism has the potential to drive $O(1)$ Sv ($1\,\text{Sv} \equiv 10^6\,\text{m}^3\,\text{s}^{-1}$) mode water formation and may be important in determining the properties of mode water in the global oceans.

1. Introduction

Mode waters are identified as a local maximum in a volumetric census in a temperature–salinity (T–S) diagram tied to a water mass with weak stratification and low potential vorticity (Hanawa and Talley 2001). The mechanism that selects the temperature, salinity, and density class where a particular mode water accumulates is not well understood. The formation of mode water has long been attributed to wintertime air–sea buoyancy loss and convection (e.g., Worthington 1959). However, because of the large thermal inertia of mode waters, their temperature is insensitive to wintertime heat loss, implying that their temperature–salinity relation is not set by air–sea fluxes (Warren 1972). Instead, processes in the ocean interior likely play a key role in the selection of their water mass properties. Mode waters are found on the equatorward side of major ocean fronts, suggesting a role for frontal processes in their generation and maintenance (Marshall et al. 2009). Thomas and Shakespeare (2015) described a mode water formation mechanism involving the mixing of cross-front temperature–salinity contrasts, cabbeling, and frontogenesis that has the potential to select the density, temperature, and salinity of a particular mode water.

The fronts that border mode waters are characterized by density-compensated temperature and salinity

Corresponding author: C. J. Shakespeare, callum.shakespeare@anu.edu.au

DOI: 10.1175/JPO-D-17-0001.1

contrasts that decrease in magnitude with depth. Along-isopycnal mixing of the disparate water masses across the fronts leads to an increase in density of the water through cabbeling (McDougall 1987). Cabbeling has been invoked to explain the formation of water masses such as North Pacific Intermediate Water (Talley and Yun 2001) and intermediate, deep, and bottom waters in the Southern Ocean (Foster 1972; Klocker and McDougall 2010; Urakawa and Hasumi 2012; Groeskamp et al. 2016). Thomas and Shakespeare (2015) posited that cabbeling could also generate mode waters at fronts because the vertical structure of the cross-front T–S contrast makes cabbeling-driven diapycnal mass fluxes convergent and prone to filling isopycnal layers over time. Their theory explored the steady-state behavior of this process in which mixing is balanced by frontogenetic strain (e.g., caused by confluent flow on the gyre- or mesoscale) that squeezes together isotherms and isohaline surfaces, thereby sustaining the cross-front T–S gradient. In this limit, the diapycnal mass flux scales with the strain, the equilibrated width of the front, and the square of the isopycnal cross-front temperature contrast. The theory predicts that mode water should form in the isopycnal layer where the magnitude of the diapycnal gradient of the cross-front temperature contrast squared is largest. In the theoretical model, however, the volume of isopycnal layers does not change in time because the frontogenetic strain is spatially uniform. While the theory illustrates how cabbeling selects the mode water isopycnal layer, since the layer never actually fills, it cannot be used to predict the temperature and salinity of the mode water that results. Moreover, the theory parameterizes cross-front mixing with a constant, lateral turbulent diffusivity and therefore greatly simplifies the submesoscale mixing processes that allow cabbeling to occur. In this article, we extend the theory of Thomas and Shakespeare (2015) using numerical simulations configured with a more realistic flow with spatially variable strain and capable of resolving submesoscale instabilities, with the goal to elucidate the underlying physics that determines the T–S relation of mode waters when they are formed through cabbeling and frontogenesis.

2. Model configuration

We use the Massachusetts Institute of Technology Global Circulation Model (MITgcm; Marshall et al. 1997) to simulate the hydrostatic primitive equations in a 200-km^2, 1-km-deep, zonally periodic box, with a constant Coriolis parameter $f = 9 \times 10^{-5}\,\mathrm{s}^{-1}$. The hydrostatic simulations run without the creation of any density inversions and thus no convection scheme (or nonhydrostatic dynamics) is required.[1] The upper boundary is treated as an implicit free surface. The model is run at 250-m horizontal resolution, with 50 vertical levels with thicknesses ranging from 5 m at the surface to 40 m at depth. The model time step is 120 s. We employ an idealized equation of state:

$$\rho(T,S) = \rho_0\left[1 - \alpha_T(T - T_0) + \beta_S(S - S_0) + \frac{c}{2}(T - T_0)^2\right], \tag{1}$$

where the only nonlinear effect is cabbeling and we select parameters $\rho_0 = 1026.5\,\mathrm{kg\,m^{-3}}$, $\alpha_T = 2.43 \times 10^{-4}\,\mathrm{K^{-1}}$, $\beta_S = 7.46 \times 10^{-4}$, and $c = -8.34 \times 10^{-6}\,\mathrm{K^{-2}}$.[2] We initialize the model with a perfectly compensated thermohaline front in a uniformly stratified background. The initial temperature field [see Fig. 2a (below)] is set as

$$T = T_0 + \frac{N^2}{\alpha_T g}z + T_S(z) + [T_N(z) - T_S(z)]\frac{1}{2}\left\{1 + \mathrm{erf}\left[\frac{y - (L/2)}{(L/8)}\right]\right\}, \tag{2}$$

and the density field is set as

$$\rho = \rho_0 - \frac{N^2\rho_0}{g}z, \tag{3}$$

where $L = 200\,\mathrm{km}$ is the domain width, $g = 9.81\,\mathrm{m^2\,s^{-1}}$, and N^2 is the constant background stratification (see Table 1 for values). The functions $T_S(z)$ and $T_N(z)$ are the southern and northern profiles of temperature variation with depth; the difference $|T_N(z) - T_S(z)|$ is maximum near/at the surface and decays to zero at depth. For our reference configuration, we set

$$T_S(z) = \frac{\Delta T_0}{2}\exp\left[-\left(\frac{z}{h}\right)^2\right], \quad \text{and}$$
$$T_N(z) = -\frac{\Delta T_0}{2}\exp\left[-\left(\frac{z}{h}\right)^2\right], \tag{4}$$

where $h = 150\,\mathrm{m}$. Given the temperature and density fields defined by (2) and (3), the salinity field is determined from the equation of state [(1)]. Zero salt, heat, and momentum

[1] While cabbeling can create density inversions in general, in our simulations the vertical exchange or mixing of cabbeled water described in section 3c happens sufficiently quickly that inversions are avoided.

[2] Parameters are chosen to approximately match the Gulf Stream region based on a reference salinity of $S_0 = 36.05$ and reference temperature of $T_0 = 18°\mathrm{C}$. The parameter values for $\rho_0 = \rho(T_0, S_0) = 1026.5\,\mathrm{kg\,m^{-3}}$, $\alpha_T = \partial_T\rho(T_0, S_0)/\rho_0$, $\beta_S = \partial_S\rho(T_0, S_0)/\rho_0$, and c are obtained from the full nonlinear equation of state.

TABLE 1. The suite of simulations. The theoretical steady-state half-width of the front is $\Delta y = \sqrt{2\kappa_h/\gamma}$. The corresponding bulk geostrophic Richardson number [(9)] is also shown. Runs with Richardson number Ri ≥ 1 tend not to develop instabilities and therefore have relatively weaker water mass transformation (see Fig. 12). Instabilities are also suppressed by large strain.

Case	Name	κ_h ($m^2 s^{-1}$)	ν_h ($m^2 s^{-1}$)	γ (f)	N^2 ($10^{-5} s^{-2}$)	Δy (km)	Ri
1	Reference	3	10	0.01	1	2.6	0.52
2		10	10	0.01	1	4.7	1.72
3		3	20	0.01	1	2.6	0.52
4		5	5	0.01	1	3.3	0.86
5		3	5	0.01	1	2.6	0.52
6	Parabola	3	10	0.01	1	2.6	0.52
7	exp8	3	10	0.01	1	2.6	0.52
8	1/3 × strain	1	10	1/300	1	2.6	0.52
9	2 × strain	6	10	0.02	1	2.6	0.52
10	1/2 × stratification	5	10	0.01	0.5	2.4	0.43
11	2 × stratification	3	10	0.01	2	2.6	1.0
12	4 × stratification	3	10	0.01	4	2.6	2.0
13	North bias	3	10	0.01	1	2.6	0.52
14	South bias	3	10	0.01	1	2.6	0.52

flux boundary conditions are applied on the northern and southern walls of the domain. Periodic boundary conditions are applied to all fields in the zonal direction.

A schematic of the mass transformation mechanism described by Thomas and Shakespeare (2015) is shown in Fig. 1. The mechanism requires the presence of a large-scale, cross-frontal confluence, such as that generated by a gyre or mesoscale eddy field, to supply water to the front and sustain cabbeling. To drive confluence across the front in our numerical model, we introduce a barotropic background flow with streamfunction ($\overline{\mathbf{u}} = -\nabla \times \overline{\psi}\mathbf{k}$)

$$\overline{\psi}(x,y) = -\frac{\gamma L^2}{4\pi^2}\sin\left(\frac{2\pi x}{L}\right)\sin\left(\frac{2\pi y}{L}\right), \tag{5}$$

which serves as an idealized representation of four barotropic eddies (shown on Fig. 2a). The constant γ is the maximum strain rate. Near the center of the domain ($x = y = L/2$), this strain field exactly matches the strain field used in the two-dimensional theory of Thomas and Shakespeare (2015) and drives meridional confluence across the zonal front. The strain field [(5)] is an exact solution to the (inviscid) primitive equations with corresponding pressure field:

$$\overline{p} = -\rho_0\left\{-f\overline{\psi} + \frac{\gamma^2 L^2}{16\pi^2}\left[\sin^2\left(\frac{2\pi x}{L}\right) + \sin^2\left(\frac{2\pi y}{L}\right)\right]\right\}. \tag{6}$$

Substituting $\mathbf{U} = \mathbf{u} + \overline{\mathbf{u}}$ and $P = \overline{p} + p$[3] into the primitive equations yields, without approximation, equations for the perturbation fields:

$$\frac{\partial \mathbf{u}}{\partial t} + \mathbf{u}\cdot\nabla\mathbf{u} + f\mathbf{k}\times\mathbf{u} + \overline{\mathbf{u}}\cdot\nabla\mathbf{u} + \mathbf{u}\cdot\nabla\overline{\mathbf{u}} = -\frac{1}{\rho_0}\nabla p + \frac{g(\rho_0-\rho)}{\rho_0}\mathbf{k} + \nabla\cdot\boldsymbol{\nu}\nabla\mathbf{u}, \tag{7a}$$

$$\frac{\partial T}{\partial t} + \mathbf{u}\cdot\nabla T + \overline{\mathbf{u}}\cdot\nabla T = \nabla\cdot\boldsymbol{\kappa}\nabla T, \tag{7b}$$

$$\frac{\partial S}{\partial t} + \mathbf{u}\cdot\nabla S + \overline{\mathbf{u}}\cdot\nabla S = \nabla\cdot\boldsymbol{\kappa}\nabla S, \quad \text{and} \tag{7c}$$

$$\nabla\cdot\mathbf{u} = 0, \tag{7d}$$

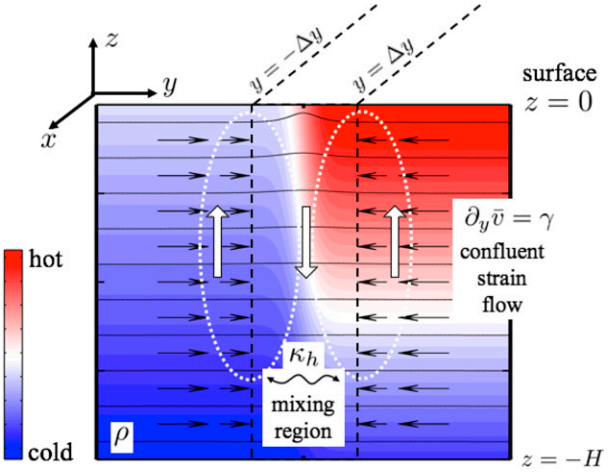

FIG. 1. Schematic of the cabbeling mass transformation mechanism of Thomas and Shakespeare (2015). A fully compensated T–S front (temperature shown in color) is oriented along the x axis, with a strain flow driving confluence across it. Cabbeling leads to the formation of a dense filament along the front (black lines denote isopycnals) and associated downwelling (circulation indicated by the white arrows). Horizontal mixing in the front and advection by the strain flow balance to a give a steady state with frontal half-width $\Delta y = \sqrt{2\kappa_h/\gamma}$ and sustained mass transformation.

[3] Uppercase P denotes the net field, $\overline{p}$ denotes the background field defined by (6), and lowercase p denotes the perturbation field and similarly for velocity.

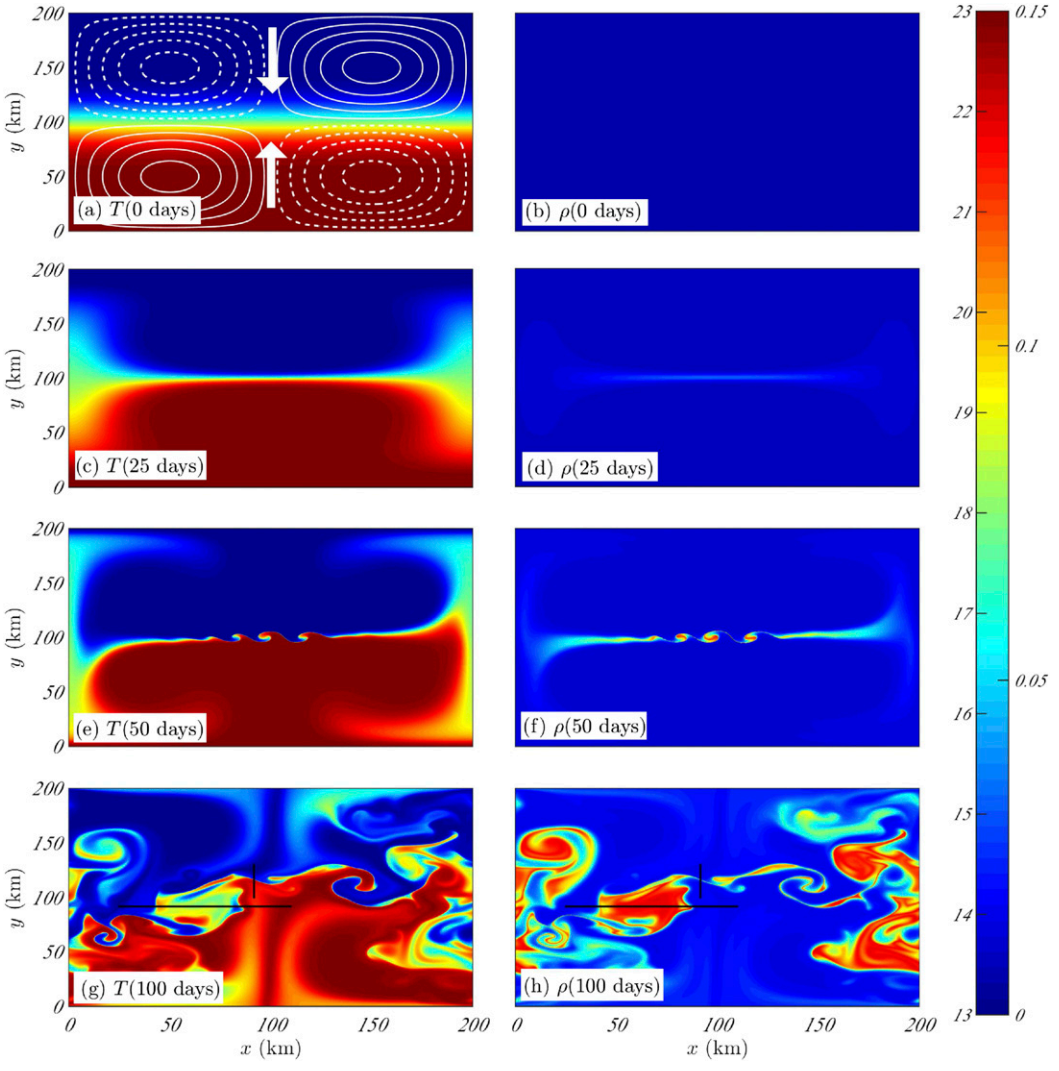

FIG. 2. Snapshots of (left) surface temperature (°C) and (right) density anomaly ($\Delta\rho = \rho - \rho_0\,\mathrm{kg\,m^{-3}}$) at 0, 25, 50, and 100 days in the reference simulation. The background flow streamfunction is superimposed in (a) with solid lines denoting anticlockwise flow, and dashed lines denoting clockwise flow. Black lines in (g) and (h) indicate the location of vertical slices shown in Fig. 3.

where $\boldsymbol{\nu}$ is the turbulent viscosity, and $\boldsymbol{\kappa}$ is the turbulent heat–salt diffusivity (tensors). In the present model, only a spatially uniform horizontal viscosity ν_h and diffusivity κ_h are applied. With only horizontal diffusivity and the simplified equation of state [(1)], it may be shown from (7) that the density evolves as

$$\frac{D\rho}{Dt} = \frac{\partial\rho}{\partial t} + (\mathbf{u} + \overline{\mathbf{u}}) \cdot \nabla\rho = \kappa_h \nabla_h^2 \rho - c\rho_0 \kappa_h |\nabla_h T|^2 . \quad (8)$$

The background flow forces the system through the additional advection terms (e.g., $\overline{\mathbf{u}} \cdot \nabla\mathbf{u}$) in (7) that are added as external forcing terms in the numerical model. In the absence of cabbeling [$c = 0$ in (1)], temperature and salinity are advected horizontally by the barotropic background flow within the uniformly stratified fluid (i.e., within an isopycnal layer), and there is no change in density [all terms in (8) are zero]. The solution to (7a) is thus $\mathbf{u} = 0$, and no perturbation flow develops. The temperature and salinity ultimately reach a steady state of advective–diffusive balance defined by $\overline{\mathbf{u}} \cdot \nabla_h T = \kappa_h \nabla_h^2 T$ for temperature (and similarly for salinity). However, in the presence of cabbeling, the temperature gradients, which are enhanced by the confluence of the background flow, drive the creation of a dense filament as per (8) along the thermohaline front. Associated with the dense filament and its horizontal density gradients, there is a corresponding geostrophic flow and vertical circulation

(indicated in Fig. 1), as described by the theory of Thomas and Shakespeare (2015).

For a surface temperature difference of ΔT_0 across the front, Thomas and Shakespeare (2015) show that the density anomaly of the filament is $\Delta\rho_0 = \rho_0(-c)\Delta T_0^2/8$. The half-width of the filament is set by a balance between the confluence and mixing, $\Delta y = \sqrt{2\kappa_h/\gamma}$, for horizontal diffusivity κ_h and strain γ as shown in Fig. 1. Here, we will show that when/if the filament becomes sufficiently sharp and dense, baroclinic submesoscale instabilities are generated along the front, which drive greatly enhanced mixing and water mass transformation. Approximately, the criterion for instability is that the bulk geostrophic Richardson number

$$\mathrm{Ri} = \frac{N^2}{\left(\frac{g}{f\rho_0}\frac{\Delta\rho}{\Delta y}\right)^2} = 128\frac{\kappa_h}{\gamma}\left(\frac{fN}{gc\Delta T_0^2}\right)^2 \tag{9}$$

is close to one, when the growth rate of ageostrophic baroclinic instability is large, namely, of the order of the inertial frequency f (Stone 1970). Here, we choose a reference strain rate of $\gamma = 0.01f = 9\times10^{-7}\,\mathrm{s}^{-1}$, which is typical of the confluence associated with large-scale ocean gyres that are characterized by velocity scales $O(1)\,\mathrm{m\,s}^{-1}$ and length scales of $O(1000)$ km. We set the diffusivity as $\kappa_h = 3\,\mathrm{m}^2\,\mathrm{s}^{-1}$, such that the dense filament (half-width $\Delta y = 2.6$ km), and any subsequent instabilities, are well resolved. We set the cross-front temperature difference as $\Delta T_0 = 10$°C and stratification as $N^2 = 10^{-5}\,\mathrm{s}^{-2}$ to obtain a bulk Richardson number for the filament of 0.52. The assumed temperature difference is larger, and the stratification smaller, than what is typical of the Gulf Stream north wall [e.g., $\Delta T_0 \sim 5$°C and $N^2 \sim 4\times10^{-5}\,\mathrm{s}^{-2}$, as used by Thomas and Shakespeare (2015)], but such values are required here in order to drive submesoscale instabilities at our idealized fully compensated front where the initial horizontal frontal density gradient is entirely due to cabbeling.

3. Results

Figure 2 shows snapshots of the surface temperature and density in the reference simulation, as described in the previous section. At time zero there is a 50-km-wide temperature (and salinity) front that is invariant in the x direction, and the density does not vary in the horizontal. The background flow field (superimposed on Fig. 2a) acts on the front, driving cross-frontal confluence between $50 < x < 150$ km and diffluence outside this region, as seen in the 25-day temperature (Fig. 2c). A filament of dense water forms in the confluent region as a result of cabbeling, as anticipated from theory. The filament continues to sharpen and densify until it becomes unstable and rolls up into eddies, as seen in the 50-day density snapshot (Fig. 2f). The eddies grow in size and are advected along the front toward the diffluent region, leading to an accumulation of mode water in this region by 100 days (Fig. 2h). A vertical transect of the vorticity, temperature, and vertical velocity through such an eddy is shown in Figs. 3a, 3c, and 3e. The cyclonic eddy (vorticity $\sim 0.1f$) is composed of a largely uniform mode water mass ($T \sim 18$°C and density anomaly $0.13 < \Delta\rho = \rho - \rho_0 < 0.15\,\mathrm{kg\,m}^{-3}$) between the surface and 100-m depth and has only weak vertical velocity on the periphery, suggesting no significant active frontogenesis.

New eddies are continually generated in the confluent region, sustaining the water mass transformation at the front. A y transect across the confluent front at 100 days is shown in Figs. 3b, 3d, and 3e. The temperature field shows the sharp front with $O(f)$ vorticity between the warm southern and cold northern water masses. The vertical velocity field possesses the structure predicted by Thomas and Shakespeare (2015) (cf. Fig. 1) with water drawn up on the sides of the density front and sinking strongly in the center as it is densified via cabbeling. This circulation is associated with a lifting of isopycnals at the front and a filling of the mode water layer ($0.13 < \Delta\rho < 0.15\,\mathrm{kg\,m}^{-3}$), which adopts a lenticular shape and strong anticyclonic flow. The mode water layer continues to deepen as cabbeling continues and ultimately the front rolls up into an eddy similar to that already described (Figs. 3a,c,e).

To clarify the mechanism of frontal instability, Fig. 4 shows the domain-integrated energy reservoirs and fluxes for the reference simulation. There are two possible inputs of energy to the domain. First, cabbeling at the front creates gravitational available potential energy (APE), computed as per Winters et al. (1995):

$$\mathrm{APE} = g\int_D \rho[z - z^*(\rho,t)]\,dV, \tag{10}$$

where z^* is the height of a fluid element of density ρ when the entire domain D is adiabatically resorted to a stable density profile. As seen in Fig. 3, cabbeling tends to form dense water near the surface above the isopycnal layer containing that density class ($z^* \sim -100$ m) and thus increases the APE of the system, as shown in Fig. 4. The second input of energy is from the background flow to the perturbation kinetic energy (KE):

$$\mathrm{KE} = \rho_0\int_D \frac{u^2+v^2}{2}\,dV. \tag{11}$$

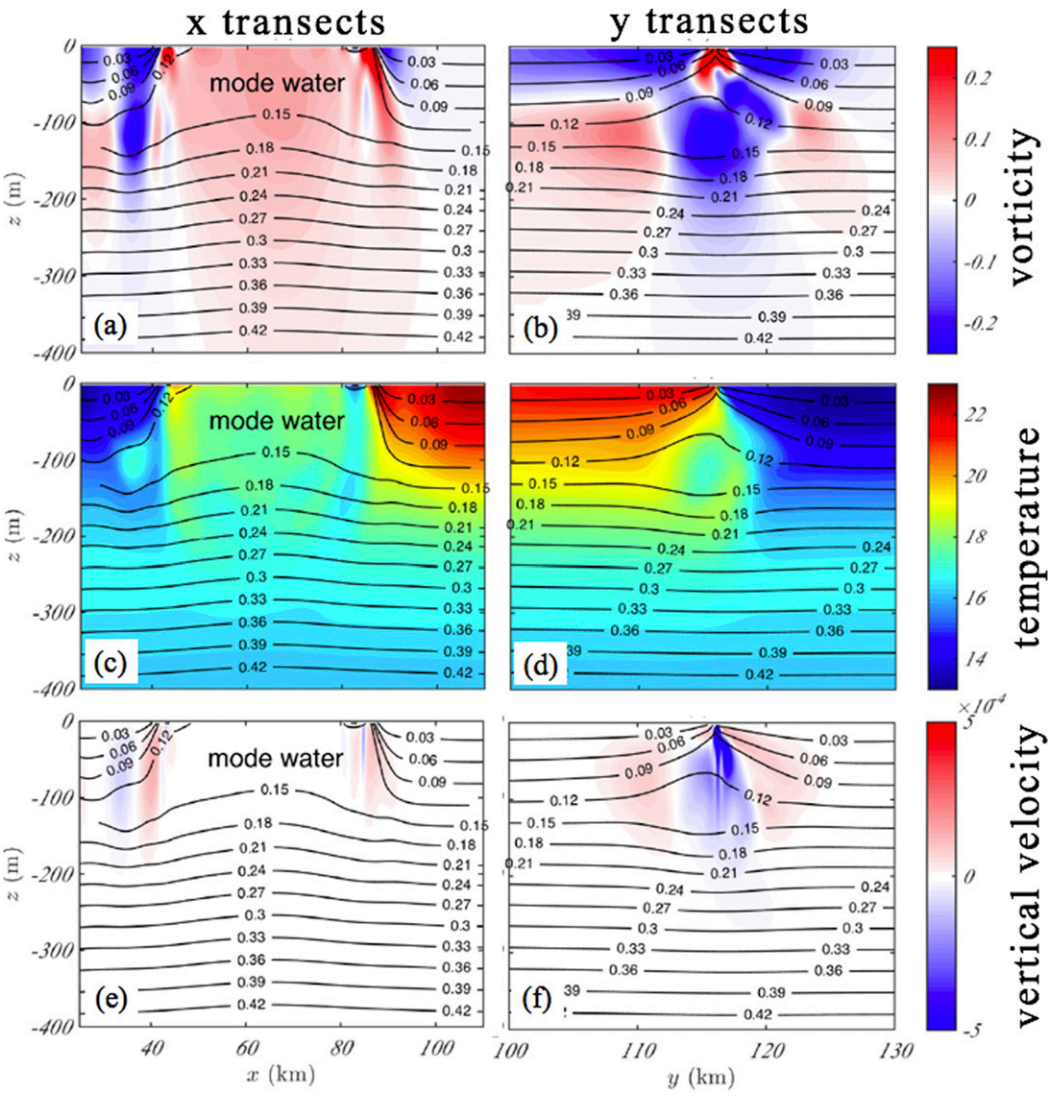

FIG. 3. Transects along the x and y slices indicated by black lines in Figs. 2g, h. (left) The x transect is across a cabbeling eddy containing accumulated mode water. (right) The y transect is across a region of strained front with active cabbeling. (a),(b) Vertical vorticity (f). (c),(d) Temperature (°C). (e),(f) Vertical velocity (m s^{-1}). Labeled black contours represent isopycnals (values shown are isopycnal anomaly $\Delta\rho = \rho - \rho_0$).

The equation for the time evolution of the kinetic energy can be computed from the momentum equation [(7a)] by taking the scalar product with $\mathbf{u}_h = (u, v, 0)$. The energy flux from the background strain flow in this equation is

$$\text{STRAIN to KE} = \rho_0 \int_D -\frac{\partial \overline{u}}{\partial x}(u^2 - v^2) - uv\left(\frac{\partial \overline{u}}{\partial y} + \frac{\partial \overline{v}}{\partial x}\right) dV. \tag{12}$$

However, given the weak strain, this source is negligible in the present simulation, except at a very late time (dotted line, Fig. 4b). The major source of kinetic energy is instead via conversion from the available potential energy ($-w\rho$, dashed line, Fig. 4b).

Prior to 50 days, the system APE increases as cabbeling creates the dense filament along the strain axis. There is negligible KE at this time as seen in Fig. 4a. However, the kinetic energy increases rapidly as the instability initiates at 50 days, implying that the eddies are drawing their kinetic energy from the available potential of the density filament, consistent with the mechanism of baroclinic instability. The eddies enhance mixing at the front, therefore amplifying cabbeling and creating more APE. The strengthening baroclinic eddies

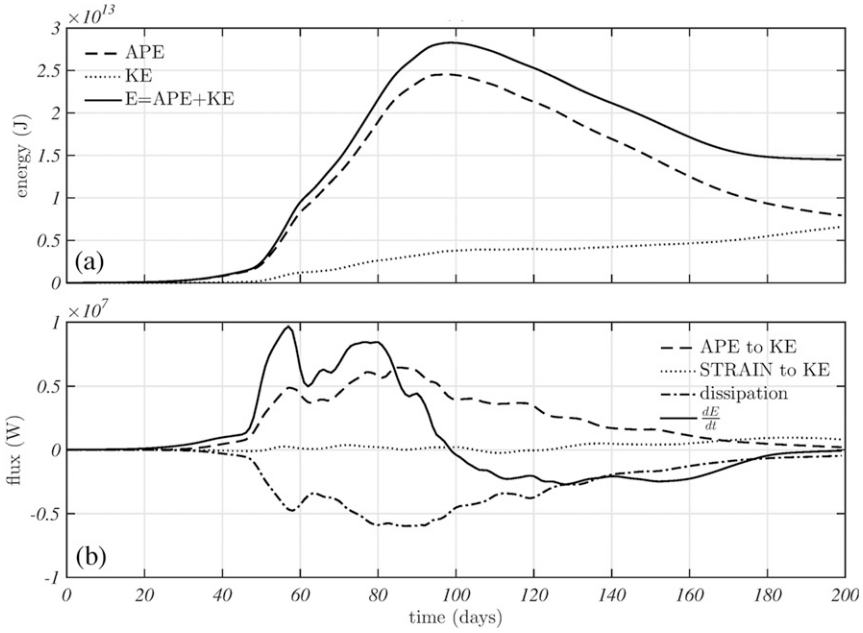

FIG. 4. Energetics of the reference simulation. (a) Energy reservoirs: gravitational APE, KE, and total mechanical energy (E = APE + KE). (b) Energy fluxes: total energy flux into system (solid), viscous dissipation (dashed–dotted), flux of kinetic energy from background flow (dotted), and conversion of available potential to kinetic energy (dashed).

continue to draw down this APE. Eventually, cabbeling weakens as the northern and southern water masses are consumed and the APE (and total mechanical energy, E = APE + KE) peaks at 97 days. There is negligible increase in the total kinetic energy between 100 and 160 days, indicating a balance between kinetic energy production via instability at the front and kinetic energy destruction via viscous dissipation. The total mechanical energy decreases consistently over this period, predominantly due to viscous dissipation (see Fig. 4b; with a contribution from irreversible mixing of density, not shown). The system energy is essentially steady by 200 days with equal APE and KE.

a. Mode water properties

The depth–density and density–temperature water mass distribution for the reference simulation is shown in Fig. 5 at 0, 100, and 200 days. At time zero, the domain is linearly stratified throughout (initial stratification is indicated by the dashed line in Fig. 5a), and the water mass is bisected into the warmer southern water and northern cooler water (dashed lines in Fig. 5d), with water in the initial front distributed between these two extremes. By 100 days (Figs. 5b,e) a maximum is visible in the water mass distribution at $\Delta\rho = 0.14 \pm 0.01\,\mathrm{kg\,m^{-3}}$, corresponding to the newly formed mode water. The maximum extends from the surface to about 125-m depth and over temperatures of 16.5° to 19.5°C. As will be shown in section 3c, this maximum in the water mass distribution is associated with the eddies seen previously in Fig. 2h. By 200 days, the initial northern and southern water masses have been completely consumed. Figure 5c shows an almost uniform density distribution over the domain, with a weakly stratified (compared to the initial state) mode water layer concentrated between 50- and 125-m depth. At this time, Fig. 5f shows that the temperature and density range of the mode water has been extended, with two distinct maxima, at the same density as previously, but with two different temperatures. The higher temperature maximum results from the mode water being fluxed around the background eddies and back into the confluent zone, where it mixes with the warmer southern water mass. Similarly, the lower temperature maximum results from the mode water being fluxed around the background eddies and back into the confluent zone, where it mixes with the cooler, northern water mass.

We now consider the question of what sets the properties of the mode water that forms in the present simulation. Thomas and Shakespeare (2015) propose that the depth at which mode water forms is determined by the inflection point in the vertical profile of cross-frontal temperature difference, that is, the value of z for which $\partial_{zz}[T_S(z) - T_N(z)]^2 = 0$. For a given temperature difference, if the two water masses bounding the front were thoroughly mixed in equal proportions at every depth,

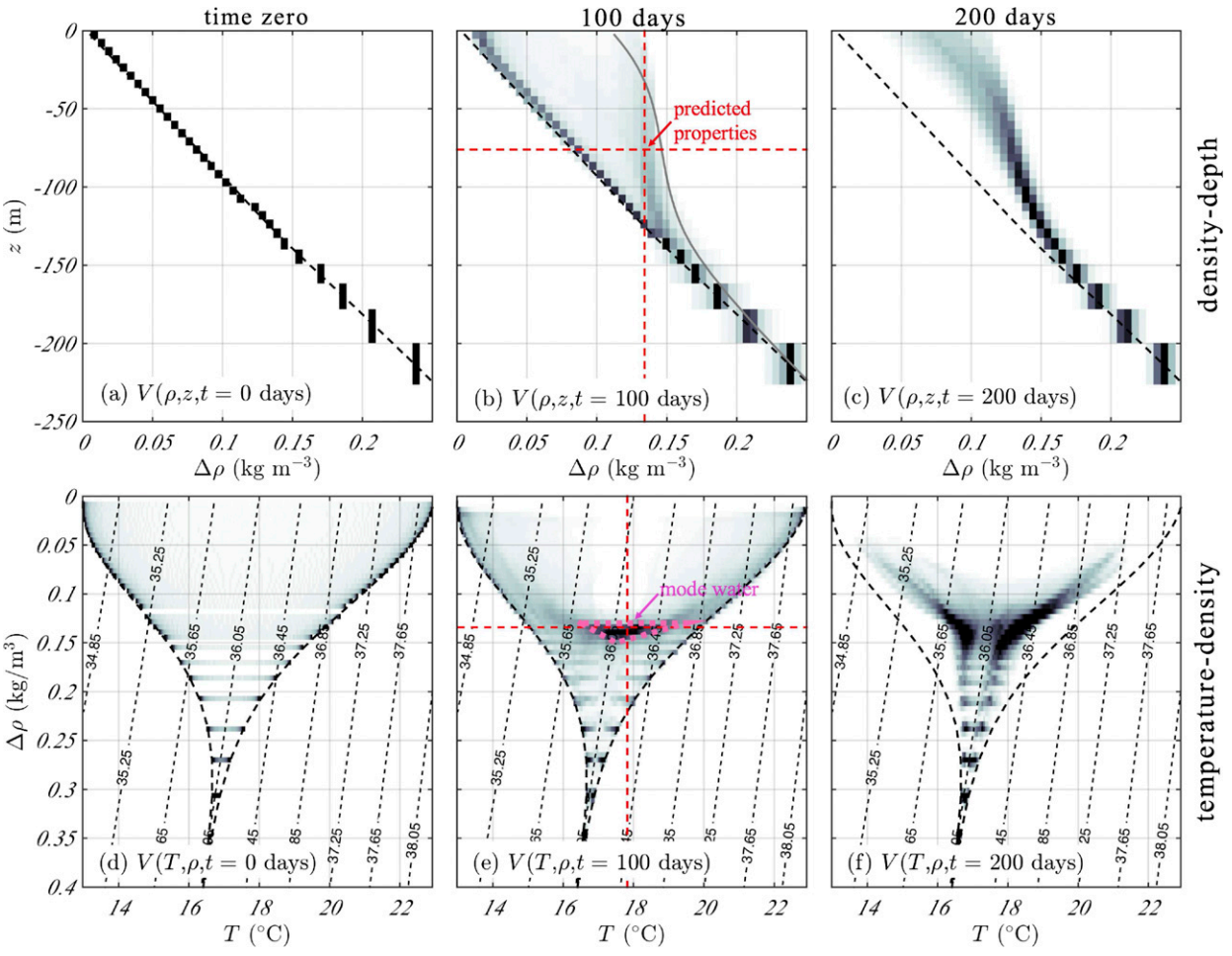

FIG. 5. Volume distribution of the water mass with time in the reference simulation. Darker colors imply a greater volume at the given location. (a)–(c) Depth–density distribution at 0, 100, and 200 days. Dashed black line shows initial (uniform) density–depth profile. (d)–(f) Density–temperature distribution at 0, 100, and 200 days. Thick dashed black lines show the initial density–temperature profile of the two water masses. Thin black lines are salinity contours (labeled). In (b), the solid gray line shows the density distribution that would result from 100% cabbeling at every depth. The theoretical depth at which mode water forms is the point of minimum stratification in this profile, shown by the horizontal red dashed line. The actual mode water density is the average density down to this theoretical depth (due to vertical mixing in the mode water eddies), shown by the vertical dashed red line. In (e), the dashed red lines indicate the predicted mode water density and temperature. The dashed pink triangle encloses the mode water region.

with no vertical exchange, the temperature profile would become

$$T_{100}(z) = T_0 + \frac{N^2}{\alpha_T g} z + \frac{1}{2}[T_S(z) + T_N(z)], \quad (13)$$

and the density profile would change from $\rho = \rho_0 - N^2\rho_0/gz$ at time zero to

$$\rho_{100}(z) = \rho_0 - \frac{N^2\rho_0}{g} z + \frac{1}{8}\rho_0(-c)[T_S(z) - T_N(z)]^2. \quad (14)$$

This 100% cabbeling density profile is shown as a solid gray line in Fig. 5b. An equivalent criterion to that of Thomas and Shakespeare (2015) is thus that mode water will be formed where the stratification associated with the 100% cabbeling density profile is minimized: $\partial_{zz}\rho_{100}(z = z_m) = 0$. For the present configuration with a Gaussian temperature difference, the corresponding depth is $z_m = -75$ m (indicated by a horizontal dashed line in Fig. 5b), which is indeed in the center of the observed mode water layer. However, unlike the linear theory of Thomas and Shakespeare (2015), where the initial uniform stratification was only weakly perturbed by cabbeling, here we observe significant changes in the vertical density structure. Thus, the density of the cabbeled water is not simply ρ_{100} at $z_m = -75$ m, as in the linear model. Instead, assume that (as will be shown

later) the cabbeled water above this depth is well mixed; then, the density of the mode water will be

$$\rho_m = \frac{1}{|z_m|}\int_{z_m}^{0} \rho_{100}(z)\,dz. \tag{15}$$

For the present Gaussian profile, the predicted density is $\Delta\rho_m = 0.134\,\mathrm{kg\,m^{-3}}$ (indicated by dashed red lines on Figs. 5b and 5e), which agrees well with the modeled mode water maximum, yet is less than the linear theory prediction of ρ_{100} because of mixing with the lighter waters above. Since the density distribution is a consequence of the mixing of temperature and salinity, the temperature of the mode water must be defined similarly to (15):

$$T_m = \frac{1}{|z_m|}\int_{z_m}^{0} T_{100}(z)\,dz. \tag{16}$$

That is, the mode water temperature is the average of the northern and southern temperature profiles for $z > z_m$. For the present profiles, the predicted temperature is $T_m = 17.8°\mathrm{C}$ (indicated by the horizontal dashed red line on Fig. 5e), which agrees well with the modeled maximum.

b. *Mass transformation rate*

Here, we investigate the rate of generation of mode water and compare with the linear theory of Thomas and Shakespeare (2015). The rate of water mass transformation may be quantified by integrating the density evolution equation [(8)] over a given isopycnal surface $A(\rho)$:

$$\begin{aligned} F(\rho) &= \int_{A(\rho)} \frac{1}{|\nabla\rho|}\frac{D\rho}{Dt}\,dA \\ &= \underbrace{\int_{A(\rho)} \frac{1}{|\nabla\rho|}\kappa_h\nabla_h^2\rho\,dA}_{F_\kappa} \underbrace{-\int_{A(\rho)} \frac{1}{|\nabla\rho|}c\rho_0\kappa_h|\nabla_h T|^2\,dA}_{F_c}. \end{aligned} \tag{17}$$

The water mass transformation thus has two components. The component purely due to diffusion F_κ acts to redistribute the water mass among density classes (it integrates to zero over the full domain) and will be discussed in section 3d. The water mass transformation due to cabbeling F_c is positive definite and is displayed in Fig. 6a for the reference simulation. The cabbeling volume flux is initially small ($F_c < 0.1$ Sv; $1\,\mathrm{Sv} \equiv 10^6\,\mathrm{m^3\,s^{-1}}$) and concentrated at light density classes ($\Delta\rho < 0.1\,\mathrm{kg\,m^{-3}}$) as the dense filament forms. When the filament becomes unstable at around 50 days, the flux increases exponentially, with the maximum flux (and flux convergence) occurring at the predicted mode water density ($\Delta\rho_m = 0.134\,\mathrm{kg\,m^{-3}}$, indicated by a dashed red line). The maximum volume flux remains above 0.4 Sv from 50 to 125 days and peaks at 0.7 Sv at 80 days. Thomas and Shakespeare (2015) predict the peak mass transformation to scale as

$$F_{c,\max} = \frac{-c\gamma_f\Delta y g\Delta T_0^2}{2\sqrt{2\pi}N_f^2}L, \tag{18}$$

where $L = 200$ km is the zonal length of the front, Δy is its width, and γ_f and N_f^2 are measures of the strain rate and stratification. This scaling assumes that the front is in a steady state where the confluent strain flow is balanced by mixing across the front, such that the surface temperature profile is

$$T = T_0 + \frac{\Delta T_0}{2}\left[1 + \mathrm{erf}\left(\frac{y - y_0}{\Delta y}\right)\right]. \tag{19}$$

In the Thomas and Shakespeare (2015) model, all the parameters in (18) were constant, but here they will vary with time as the front evolves. We extract the surface temperature difference ΔT_0 and the frontal half-width Δy from the simulation by fitting the error function profile [(19)] to the zonally averaged surface temperature in the model at a given time, shown in Fig. 6b. The fitted parameters are shown as a function of time in Figs. 6c and 6d. The fit is accurate (correlation coefficient exceeds 0.93) until about 150 days, when there is no longer a distinct single front between cold northern and warm southern water masses. The background strain rate γ_f in (18) is computed as the average strain over the width of the front, where the local strain is defined by $\partial_y\overline{v} = \partial_{xy}\overline{\psi}$ evaluated along the strain axis $x = L/2$, or

$$\gamma_f = \gamma\frac{1}{2\Delta y}\int_{L/2-\Delta y}^{L/2+\Delta y} -\cos\frac{2\pi y}{L}\,dy = \frac{\gamma L}{2\pi\Delta y}\sin\frac{2\pi\Delta y}{L}, \tag{20}$$

and thus is smaller for a wider front. Assuming a steady state, the frontal width $\Delta y = \sqrt{2\kappa_h^{\mathrm{eff}}/\gamma_f}$ from linear theory, and we thus have a scaling for the effective diffusivity that depends only on the frontal width

$$\kappa_h^{\mathrm{eff}} = \frac{\gamma L\Delta y}{4\pi}\sin\frac{2\pi\Delta y}{L} \tag{21}$$

and is shown as a function of time in Fig. 6d. The effective diffusivity peaks at over $500\,\mathrm{m^2\,s^{-1}}$ (cf. explicit diffusivity of $3\,\mathrm{m^2\,s^{-1}}$) between 75 and 115 days, suggesting that the submesoscale instabilities are driving

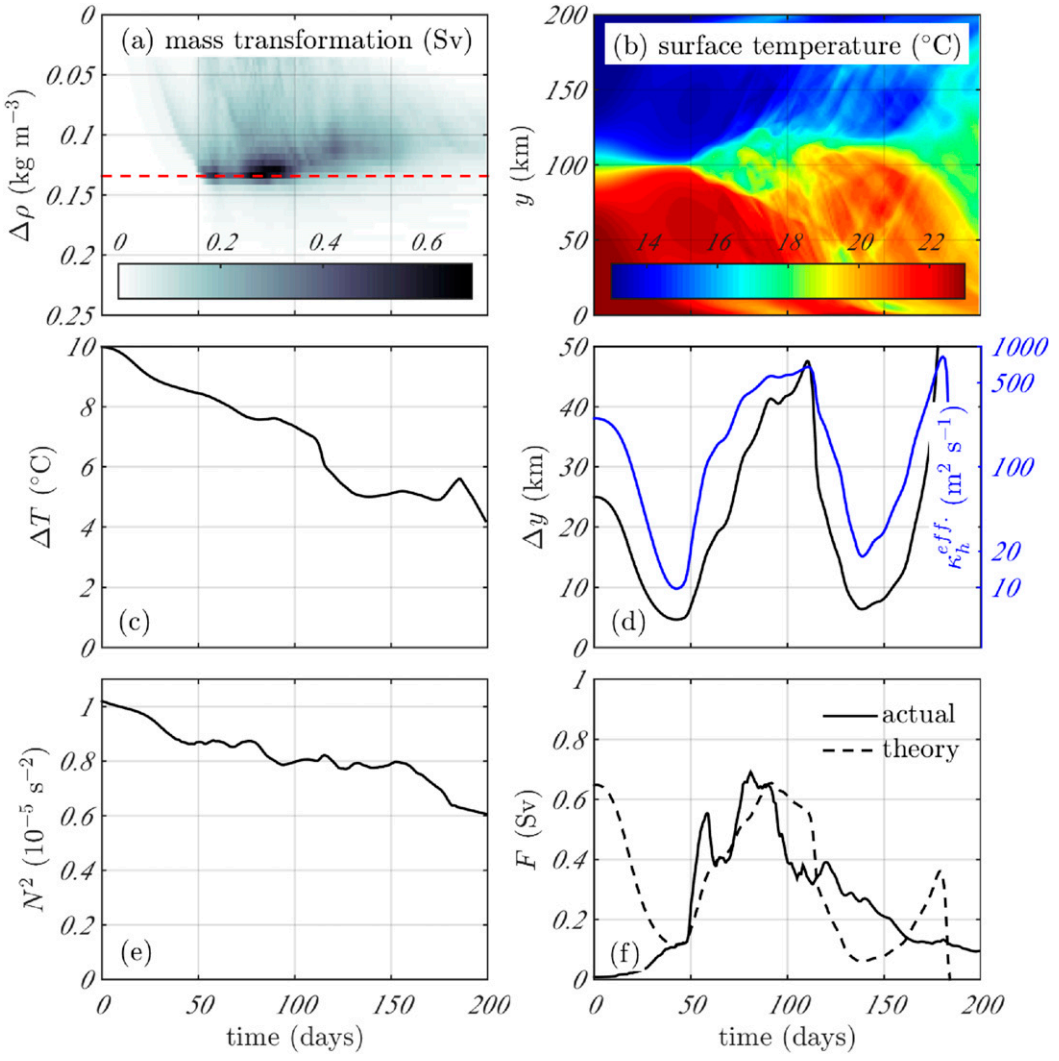

FIG. 6. (a) Water mass transformation (Sv) as a function of time and density. (b) Zonally averaged surface temperature with time. (c) Temperature difference across the front with time from error function fit. (d) Frontal half-width with time from error function fit (black) and estimated effective diffusivity κ_h^{eff} (blue). (e) Average stratification N_f^2 in the front. (f) The maximum water mass transformation (Sv) from the simulations (solid) and predicted by steady-state linear theory (dashed) using fit parameters.

very intense mixing at these times. We note that the large value of the effective diffusivity near time zero in Fig. 6d is spurious. During this time, the front is sharpening under the influence of the background strain and thus the measured width of the front is not a steady-state width due to a balance between mixing and confluence; therefore, the scaling fails. The diffusivity scaling also fails beyond 150 days when the error function fit breaks down. Similar to the strain rate, the stratification N_f^2 in (18) is computed as the mean stratification over $L/2 - \Delta y < y < L/2 + \Delta y$ and $z > -175$ m and is shown in Fig. 6e. The maximum water mass transformation predicted by the theoretical scaling [(18)] is shown in Fig. 6f along with the actual maximum value from the simulation. The theoretical scaling provides a reasonable estimate for the water mass transformation during the period of peak transformation, between 50 and 125 days. Similar to the effective diffusivity, the scaling is not valid prior to 40 days or beyond 150 days.

c. *Mode water sources*

Here, we use Lagrangian floats to investigate the sources and spatial distribution of the mode water in our simulations. As described in section 3a, the mode water is identified at 100 days as the maximum in the ρ–T–S volume distribution shown in Fig. 5e, around which we have drawn a pink-dashed triangle. Model grid points

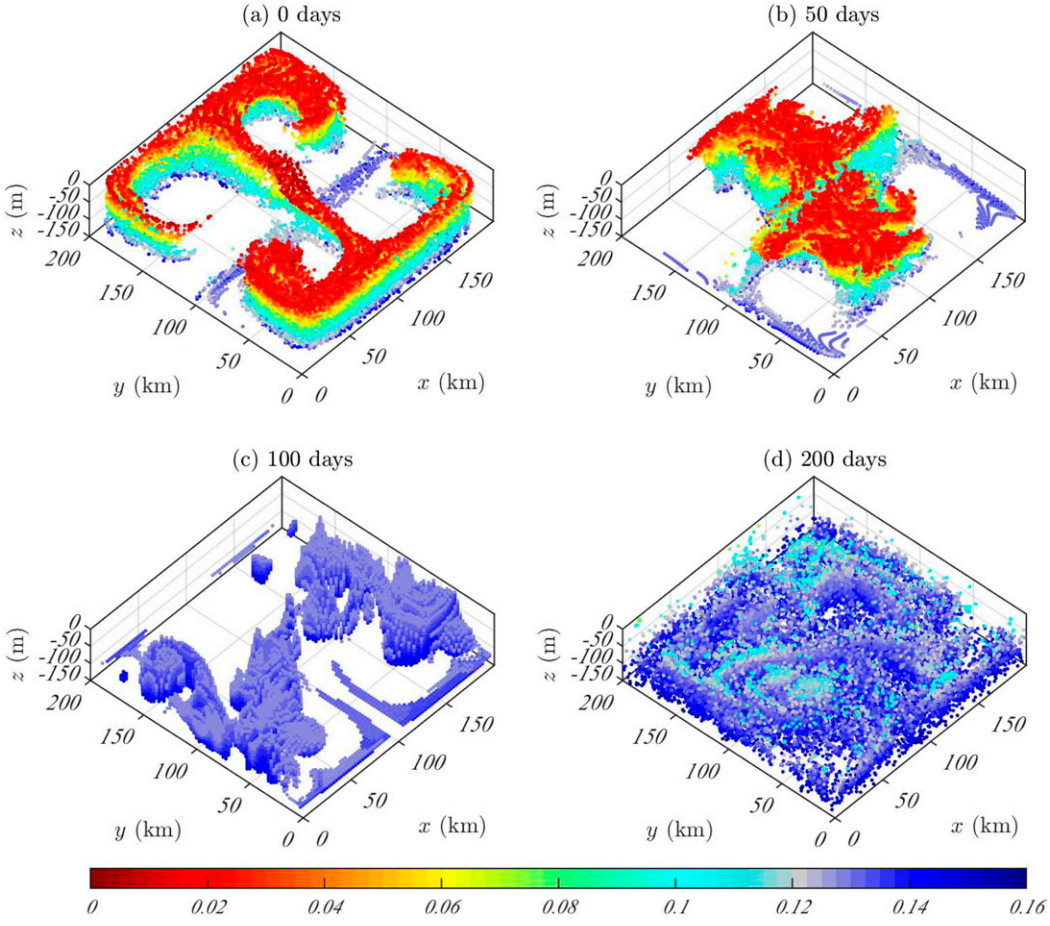

FIG. 7. Mode water parcel tracking. The mode water is defined at time 100 days as having ρ–T–S properties corresponding to the region enclosed by the pink triangle in Fig. 5e. Approximately 25 000 parcels are evenly distributed every 1.25 km in the horizontal and in each vertical level within the mode water. (a) Parcel locations at time zero obtained from backward advection. (b) Parcel locations at 50 days obtained from backward advection. (c) Parcel locations at time 100 days (when parcels are initialized). (d) Parcel locations at 200 days obtained from forward advection. Color indicates the density anomaly, $\Delta\rho = \rho - \rho_0$ (kg m^{-3}), of each parcel. The line of parcels along the front ($y = 100$ km) in (a) correspond to water within the initial front that is already in the mode water layer. The volume of this water is insignificant compared to the volume ultimately formed via cabbeling (e.g., see Figs. 5d,e).

(x, y, z) with ρ–T–S values within this triangle at 100 days are identified as locations where mode water exists. In these locations, we initialize a Lagrangian parcel at every tenth such grid point in the horizontal (which equates to one parcel in every 1.25 km $\times$ 1.25 km square within regions of mode water) and in each vertical level, leading to a total of just over 25 000 parcels. The spatial location of each parcel at the 100-day tagging time is shown in Fig. 7c, with colors indicating the density anomaly ($\Delta\rho = \rho - \rho_0$) of the parcel. The mode water parcels are located over depths from 0 to 150 m and are located within eddies, predominately in the diffluent region of the domain. As seen in Fig. 7c, these eddies are weakly stratified with a density difference of approximately 0.02 kg m^{-3} over their 150 depth, which equates to a stratification of 1.3×10^{-6} s^{-2}—an order of magnitude smaller than the background stratification ($N^2 = 10^{-5}$ s^{-2}).

We employ 3-hourly outputs of the three-dimensional model velocity fields to advect the Lagrangian parcels both forward and backward in time.[4] The locations of the parcels at time zero and 50 and 200 days are shown in

[4] A second-order Runge–Kutta method is used to advect parcels. To obtain the correct parcel paths, the total flow field (model perturbation plus imposed background eddy) must be used for the advection.

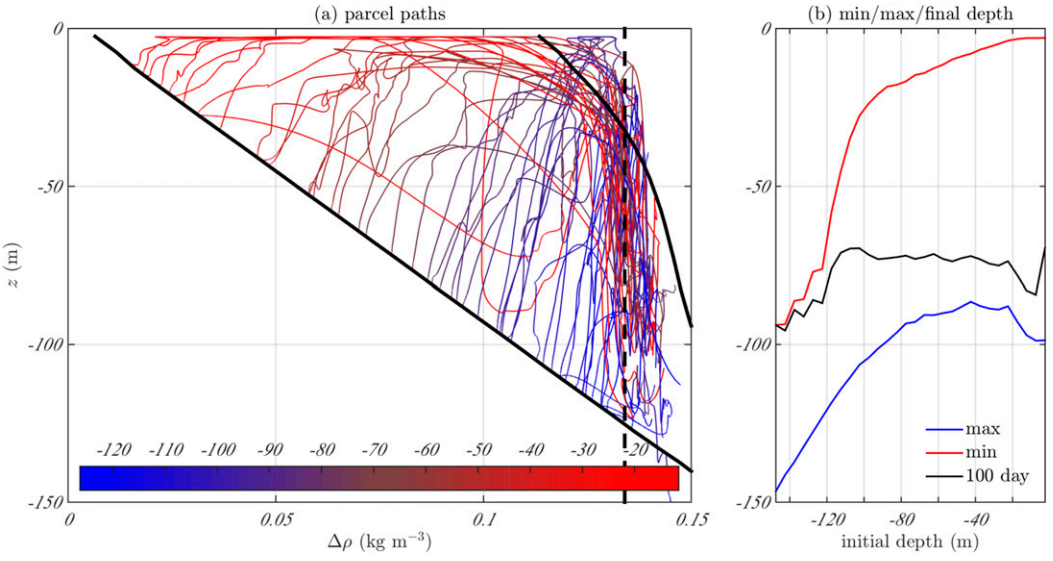

FIG. 8. (a) The paths in density–depth space of 50 parcels starting at different initial depths from 0 to 100 days. Parcel trajectories are colored according to the initial parcel depth. The straight black line shows the initial depth–density profile while the curved black line is ρ_{100}. The dashed black line indicates the mode water density. (b) The average value (over all parcels) of the minimum, maximum, and 100-day depth of a parcel for a given initial depth.

Figs. 7a, 7b, and 7d, respectively. The parcels are initially evenly distributed between the northern and southern sides of the front and over the full 0–150-m depth (0–0.16 kg m^{-3} density) range. As time proceeds the parcels are drawn in horizontally along the line of maximum confluence (x = 100 km) by the barotropic background strain flow and by 50 days have accumulated in the confluent regions on either side of the front. As the instability grows (50 to 100 days) these two stratified water masses are mixed at the front, forming the weakly stratified eddies. By 200 days the mode water has spread over most of the domain to both the north and south of the original front.

Figure 8a displays the paths of 50 parcels in density–depth space between 0 and 100 days. The 50 parcels start at different initial depths (densities) and random horizontal positions. Initially, parcels remain fixed in density–depth space as they are advected horizontally by the strain flow. As they approach the front, the parcels begin to rise (consistent with the vertical velocity field at the front; Fig. 3f) and marginally densify [density increases by O(0.01–0.03) kg m^{-3}]. However, the majority of the densification occurs as parcels reach their maximum height, with most parcels densifying to the mode water density class (0.13–0.14 kg m^{-3}) between 0- and 25-m depth. The newly densified mode water parcels then sink at the front in a vertical jet (as seen in Fig. 3f). These parcel paths are at odds with the linear model of Thomas and Shakespeare (2015), which proposed dense water formation by essentially separate horizontal mixing of water masses at each depth, after which the density of parcels reaches ρ_{100}. Instead, here we have upward advection of water to near the surface, where the vast majority of cabbeling occurs, thus producing well-mixed mode water with a density different than ρ_{100}, as argued previously. To further emphasize this behavior, Fig. 8b displays the minimum, maximum, and final (100 day) depths averaged over all parcels starting at a given initial depth (density). The mean 100-day depth of any parcel initially above 100 m is close to 75 m, regardless of its initial depth. On average, all such parcels rise to a minimum depth of 0–25 m prior to densifying and sink to a maximum depth of 90–100 m after densifying.

d. *Diffusive water mass transformation*

Heretofore, we have focused on the water mass transformation due to cabbeling only. However, the use of a horizontal diffusivity in the simulations implies that there is significant mass transformation purely due to diffusion [e.g., (17)]. This transformation occurs wherever there are horizontal gradients in density (i.e., density fronts) such as on the edge of the eddies containing the mode water. The horizontal diffusion acts to lighten the relatively higher-density, near-surface mode water and densify the relatively low-density, stratified water surrounding the eddies. This effect can be seen in the lightening of mode water parcels (to 0.1–0.12 kg m^{-3}) near the surface in Fig. 7 between 100 and 200 days. To quantify the net effect of diffusive transformation, Fig. 9

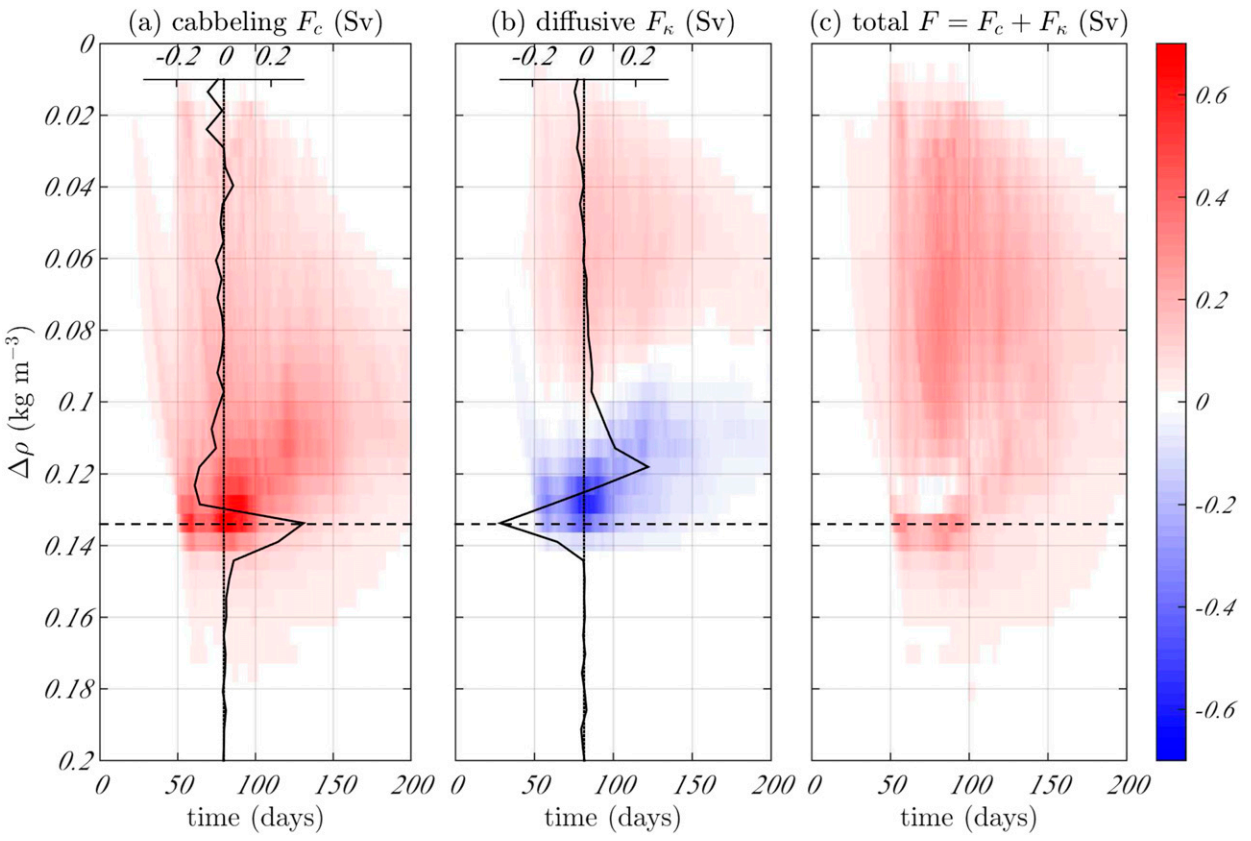

FIG. 9. The water mass transformation at a given density and time due to (a) cabbeling, (b) diffusion, and (c) both effects as defined by (17). The volume flux divergence $-(\partial F/\partial\rho)\Delta\rho$ (Sv) for isopycnal layers of width $\Delta\rho = 0.005$ kg m^{-3} at 80 days is overlaid in (a) and (b). The predicted mode water density is indicated by the dashed black line.

displays the water mass transformation from both cabbeling (as shown previously; Fig. 6) and diffusion and their sum (the total transformation). Figure 9b implies that diffusion is removing volume from around the 0.134 kg m^{-3} mode water created via cabbeling (maximum volume flux divergence) and fluxing it into the 0.1–0.12 kg m^{-3} layer (maximum volume flux convergence), exactly as observed in Fig. 7. However, this "leakage" to lighter density classes does not affect the essential mechanism of mode water formation via cabbeling, as described in previous sections. Instead, the diffusion tends to modify the density of the mode water after it has been created by cabbeling.

e. Sensitivity

Here, we investigate the sensitivity of the mode water properties to the initial water mass distribution (section 1) and rate of mass transformation to various model parameters such as stratification, strain, viscosity, and diffusivity (section 2). In addition to the reference case discussed previously, there are a further 13 simulations described in this section, which are summarized in Table 1.

1) TEMPERATURE–DEPTH STRUCTURE

In section 3a, we proposed a method to determine a priori the properties of the mode water generated in our simulations. Here, we show that this method is robust for various initial water mass distributions.

The reference simulation has a vertical temperature variation that is evenly balanced between the northern and southern sides of the front [(4)]. Instead, here we consider a case where the variation is biased to the northern (cold) side:

$$T_S(z) = 0, \quad \text{and} \quad T_N(z) = -\Delta T_0 \exp\left[-\left(\frac{z}{h}\right)^2\right]. \qquad (22)$$

Since the net temperature difference with depth $|T_N(z) - T_S(z)|$ is unchanged, the density of the mode water will be unchanged, but the temperature and salinity will change. Equation (16) predicts that the temperature of the mode water for the north-biased profile will be 13.3°C or 4.5°C cooler than the reference case. The 100-day water mass distribution for the north-biased simulation is shown in Fig. 10a, alongside the water mass

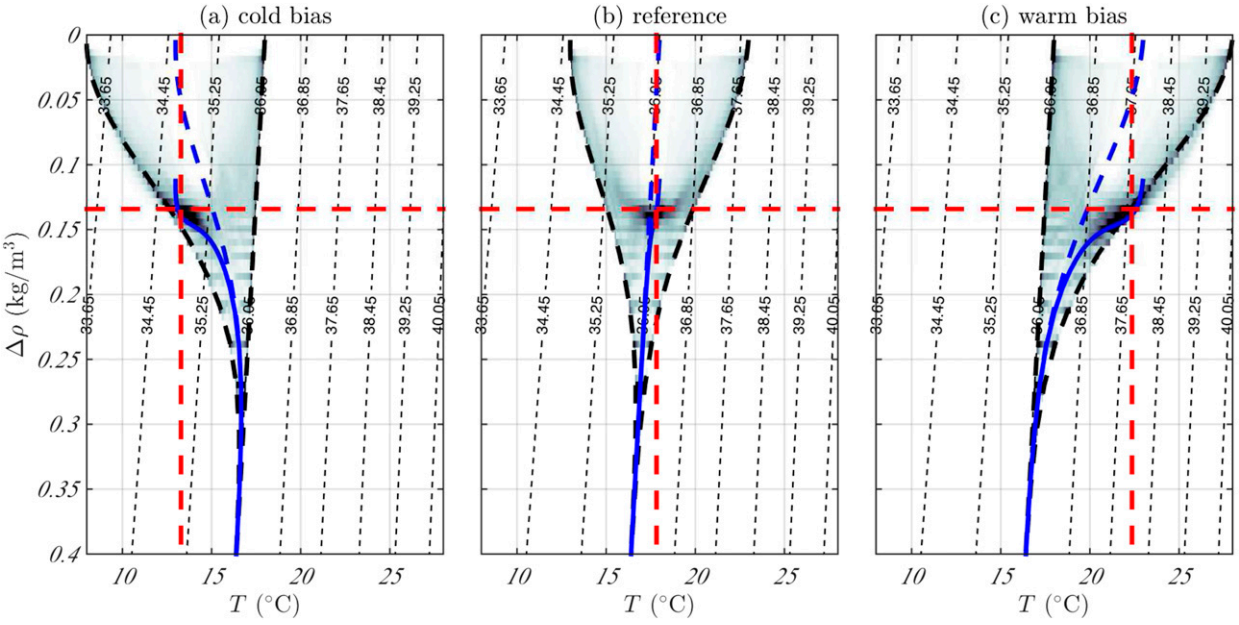

FIG. 10. Comparison of mode water formation for three different initial water mass distributions. Plots show the water mass volume distribution at 100 days with darker colors indicating greater volume. (a) All temperature anomaly variation on the cold side. (b) Evenly balanced, as in previous figures. (c) All variation on the warm side. Mode water formation is biased toward the side with the greatest temperature variation with depth (density). Red dashed lines indicate the predicted mode water density and temperature in each case, as described in the text. Dashed blue lines show the temperature T_{100} [(16)] of the evenly (horizontally) mixed mode water mass plotted against the initial density. Solid blue lines show the same temperature but plotted against the 100% cabbeling profile ρ_{100}.

distribution for the reference case (Fig. 10b). Equation (16) accurately predicts the mode water temperature. We perform the same experiment for a south-biased temperature profile:

$$T_S(z) = \Delta T_0 \exp\left[-\left(\frac{z}{h}\right)^2\right], \quad \text{and} \quad T_N(z) = 0, \tag{23}$$

as shown in Fig. 10c. Once again, mode water temperature is accurately predicted.

The 100% cabbeling temperature profile T_{100} [(13)] is shown in blue on each subplot in Fig. 10 plotted against the initial density of the water mass [dashed; equivalent to depth since $\rho_{\text{init}} = \rho_0(1 - N^2 z/g)$] and against ρ_{100}, the 100% cabbeling density profile (solid). The change in density due to cabbeling corresponds to the height difference between the two lines. Since the increase in density is greatest for the greatest temperature differences (at the surface) and reduces with depth, cabbeling leads to a contraction in the density range of the near-surface water mass and hence an accumulation of "mode water" at a particular density class. When the temperature–depth profiles of the two source water masses are not evenly balanced, the mean temperature T_{100} also varies strongly with density (depth). For the cold-biased case, T_{100} increases strongly with depth (initial density). Thus, when the near-surface water mixes to temperature T_{100} and densifies to ρ_{100}, it lies close to the cold source water T–ρ profile at depth (solid blue line on Fig. 10). The reverse is true for the warm-biased case. It is apparent in both temperature-biased simulations that the mode water distribution does not precisely match the $\rho_{100}(T_{100})$ profile; specifically, the density and temperatures ranges of the observed mode water are reduced compared to what is implied by this profile. The reason is that this profile assumes that the mixing in the simulations is purely horizontal, which is not the case, as was demonstrated in section 3c. Instead, the frontal circulation drives a vertical mixing of all the cabbeled water, further contracting the temperature and density range of the water and causing the distinct mode water maxima in the volume distribution (Fig. 10).

Now we consider whether our method accurately predicts mode water properties for different (non-Gaussian) vertical profiles of temperature difference. We consider two additional profiles: the "exp8" profile,

$$T_S(z) = \frac{\Delta T_0}{2} \exp\left[-\left(\frac{z}{h}\right)^8\right], \quad \text{and}$$
$$T_N(z) = -\frac{\Delta T_0}{2} \exp\left[-\left(\frac{z}{h}\right)^8\right], \tag{24}$$

where $h = 150$ m, and the "parabola" profile,

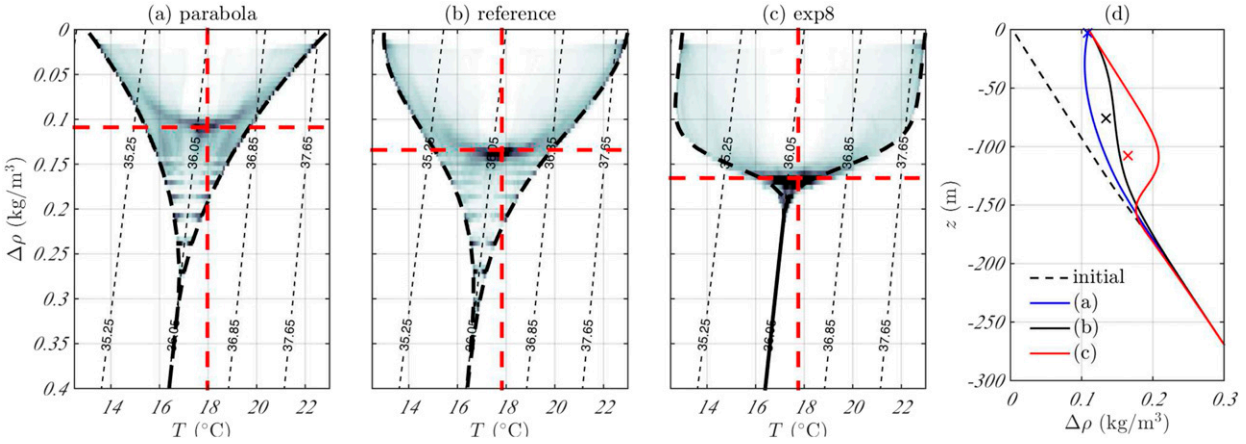

FIG. 11. Comparison of mode water formation for three different initial temperature–depth profiles. (a) Parabola profile (120 days), (b) reference Gaussian profile (100 days), (c) exp8 profile (100 days). (a), (b), and (c) show the water mass volume distribution with darker colors indicating greater volume. Red dashed lines indicate the predicted mode water density and temperature in each case, as described in the text. (d) The initial depth–density profile (dashed black) and the profiles that would result in each case (a)–(c) from 100% cabbeling at every depth. The theoretical depth of mode water formation is the point of minimum stratification in this profile: (a) surface, (b) 75 m, and (c) 108 m. As mode water is well mixed, the density of the water can be calculated as the average of the theoretical profiles above these depths. The predicted depth and density is shown by an X for each case.

$$T_S(z) = \frac{\Delta T_0}{2}\left(\frac{z}{h}+1\right)^2 H(z+h), \quad \text{and}$$
$$T_N(z) = -\frac{\Delta T_0}{2}\left(\frac{z}{h}+1\right)^2 H(z+h), \tag{25}$$

where $h = 300\,\text{m}$, and H is the Heaviside function. The 100% cabbeling density profiles [(14)] for these two configurations are shown in Fig. 11d. Both density profiles imply a negative stratification at some depth, which is clearly unphysical. Thus, instead of seeking the minimum stratification as the depth of mode water formation, as argued previously, we refine our criterion to be that the depth z_m of mode water formation is where $\partial_{zz}\rho_{100} = 0$ if $\partial_z\rho_{100}$ is everywhere negative, and the depth at which $\partial_z\rho_{100}$ is first greater than zero otherwise. For the parabolic profile $\partial_z\rho_{100}$ is positive at the surface, so $z_m = 0\,\text{m}$. For the exp8 profile, $\partial_z\rho_{100}$ goes to zero at $z_m = 108\,\text{m}$ depth. The mode water density is then computed as the average of ρ_{100} above this depth as previously [(15)]. The water mass distributions for the parabola and exp8 profiles are shown in Figs. 11a and 11c, respectively, alongside the reference case (Fig. 11b). The predicted mode water density (and temperature) is indicated by red, dashed lines and show good agreement with the observed maxima in the water mass distributions. The mode water density anomaly is $0.165\,\text{kg m}^{-3}$ for the exp8 profile but only $0.109\,\text{kg m}^{-3}$ for the parabola profile; thus, the mode water density anomaly can vary by over 50% for the same cross-frontal temperature difference, purely as a result of different temperature structure with depth.

2) MODEL PARAMETERS

The values' horizontal diffusivity ($\kappa_h = 3\,\text{m}^2\,\text{s}^{-1}$) and viscosity ($\nu_h = 10\,\text{m}^2\,\text{s}^{-1}$) in the reference simulation are "subgrid turbulent" parameters whose values are chosen to prevent the collapse of gradients below the grid scale. As such, it is of interest to determine the sensitivity of our results and in particular the rate of water mass transformation via cabbeling to these parameters. Figure 12 displays the maximum water mass transformation with time (Fig. 12a) and cumulative water mass transformation across all density classes (in units of domain volume; Fig. 12b) for five simulations with different viscosity and/or diffusivity. The reference simulation is shown in black. Simulations where only the viscosity is varied are shown as dashed curves. The water mass transformation tends to decrease with increased viscosity, presumably due to the instabilities being partially suppressed. The same effect is seen for increased diffusivity; that is, increased explicit mixing (diffusivity) has the effect of reducing the net mixing by preventing sharp gradients and the generation of the instabilities responsible for this mixing. For $\kappa_h = 5\,\text{m}^2\,\text{s}^{-1}$ (blue), the growth of the instability is delayed by about 25 days, and for $\kappa_h = 10\,\text{m}^2\,\text{s}^{-1}$ (red), the instability is entirely suppressed. These results suggest that reducing the viscosity and/or diffusivity toward more realistic values (e.g., by using a higher-resolution model) will either not change, or possibly increase, the rate of water mass transformation.

Figures 12c and 12d display analogous plots of water mass transformation for simulations with 0.5, 2, and 4

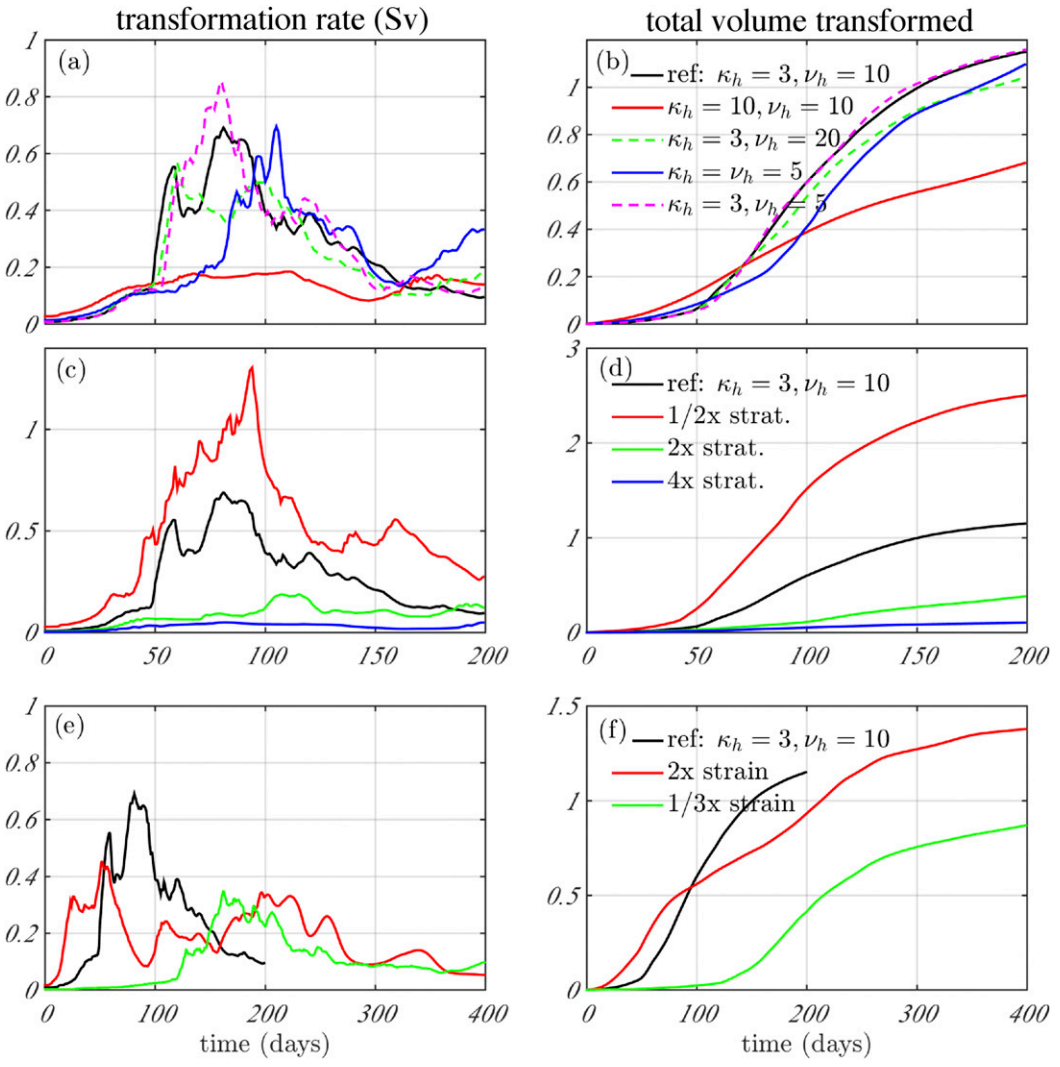

FIG. 12. Sensitivity of solution to (a),(b) viscous and diffusive parameters, (c),(d) background stratification, and (e),(f) background strain. (left) Maximum water mass transformation (F; Sv) with time. (right) Cumulative water mass transformation across all density classes, in units of domain volume (4×10^{13} m^3).

times the background stratification used in the reference case. The half-stratification case also has an increased horizontal diffusivity ($\kappa_h = 5\,\mathrm{m^2\,s^{-1}}$; see Table 1), which is necessary to keep the Richardson number [(9)] above 0.25 and thereby prevent poorly resolved frontal shear instabilities. Thomas and Shakespeare (2015) predict that the water mass transformation scales inversely with the stratification, which is largely consistent with these simulations. In particular, halving the stratification (red) results in a more-than-doubled peak water mass transformation of 1.3 Sv. The case with doubled stratification (green) has a Richardson number of Ri = 1.0 (see Table 1) and so is only weakly unstable, leading to a peak water mass transformation of less than 0.2 Sv. The case with 4 times stratification has Ri = 2 and does not manifest an instability, leading to negligible transformation.

Last, in Figs. 12e and 12f, we show the water mass transformation for simulations with 1/3 and 2 times the reference background strain. In each simulation the reference diffusivity is modified by the same factor (i.e., 1/3, 2) to keep the frontal width and Richardson number unchanged. Both the larger and smaller strains result in less water mass transformation than the reference simulation. This behavior appears to be the result of two competing effects: (i) increasing the strain increases the supply of water to the front, which should increase water mass transformation, but (ii) increasing the strain rate also tends to suppress instabilities at the front (Bishop 1993; Spall 1997), thus reducing the amount of mixing.

4. Application to observed mode waters

We now analyze the water mass properties of observed mode waters near the Kuroshio, Gulf Stream, and Subantarctic Front to evaluate the potential relevance of cabbeling, mixing, and frontogenesis to their formation. The observations are from WOCE line P10 in the North Pacific (cruise expedition designation 49NZ20050525), WOCE line A22 in the North Atlantic (cruise expedition designation 316N200310), and the OISO-01 cruise at the Subantarctic Front to the northeast of Kerguelen Island (Lo Monaco and Metzl 2007). At each front, the cross-front temperature contrast ΔT_f decreases with density near the isopycnal layers of each mode water (Fig. 13). The theory predicts that cabbeling and frontogenesis should therefore drive a water mass transformation [(18)] that is convergent in these density classes. For constant strain and mixing, the maximum mode water formation occurs in the isopycnal layer where the diapycnal gradient of $(\Delta T_f)^2$ is largest in magnitude. This isopycnal layer (indicated by the dashed lines in Fig. 13) was calculated using the observed cross-front temperature contrasts at each front and compares favorably with the actual density class of the mode waters.

Interestingly, the temperatures of the observed mode waters all exceed the temperature T_{100} that would result if the water masses that bound the fronts were mixed isopycnally in equal proportions (e.g., dotted lines in Fig. 13). They are instead very similar to the temperatures of the water masses on the warm side of the fronts. As described in section 3e, this does not, however, rule out cabbeling as a potential mechanism for their formation. The temperature profiles at the three fronts are all biased to the warm water mass; therefore, a combination of cross-front and vertical mixing could allow cabbeling to generate mode waters with similar properties to the warm water mass, in an analogous fashion to what is seen in our simulations. Having said this, there are processes present in the ocean that are absent in our simulations that could shape the formation of mode waters at observed fronts. We will discuss these potential limitations of our model and opportunities for future research in the next section.

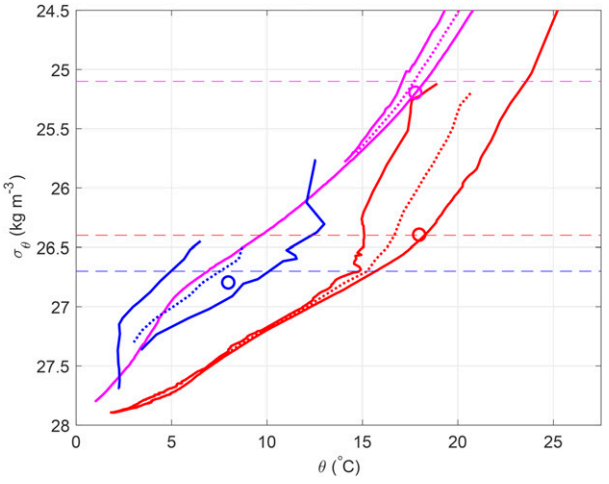

FIG. 13. Observed profiles of potential temperature at pairs of hydrographic stations that straddle the Gulf Stream (red solid), Kuroshio (magenta solid), and the Subantarctic Front northeast of Kerguelen Plateau (blue solid) and the temperature and potential density of the mode waters that are found in each region (circles). The density class where the cabbeling-driven mode water formation is largest based on the cross-front temperature difference at each front is indicated by the dashed lines. The temperature profile that would result if the two water masses across the fronts were mixed isopycnally in equal proportions T_{100} is denoted by the dotted lines.

5. Discussion

Here, we have investigated the formation of mode water via cabbeling in an idealized simulation of a strained thermohaline front. We initialized the simulation in a uniformly stratified state and imposed a balanced background flow field consisting of four mesoscale eddies driving a confluent strain rate of $O(10^{-6})\,\mathrm{s}^{-1}$ across the front. The background flow draws cold northern and warm southern water into the front, where horizontal mixing results in the formation of a dense filament via cabbeling, as predicted by Thomas and Shakespeare (2015). Here, we have selected parameters such that this filament is baroclinically unstable, as is the case for thermohaline fronts such as the Gulf Stream north wall. The submesoscale baroclinic instabilities at the front drive enhanced horizontal mixing with effective diffusivities of $O(100)\,\mathrm{m}^2\,\mathrm{s}^{-1}$, exceeding the explicit diffusivity in the simulations by two orders of magnitude. This turbulent mixing causes significant water mass transformation at the front with peak values of $O(0.5\text{–}1)$ Sv for the 200-km-long front, consistent with the theoretical prediction [(18)] of Thomas and Shakespeare (2015). The resolved turbulent mixing is strengthened, and the water mass transformation increases as the explicit viscosity or diffusivity in the model is reduced, suggesting our results are robust and are not a consequence of artificially high turbulent parameters.

Unlike classical mechanisms of mode water formation, which rely on air–sea fluxes, the cabbeling mechanism investigated here prescribes the temperature and salinity of the mode water, given knowledge of the temperature–salinity profiles with the depth of the source water masses on either side of the front. Key to

this mechanism is that mode water formation by the submesoscale instabilities is a fundamentally three-dimensional process. Essentially all water mass transformation in the simulations occurs in the surface 25 m, with water from as deep as 125 m being drawn up to the surface prior to transformation. The mode water forms at the front above 25 m and then sinks to fill the mode water layer at depth. This layer gradually expands up to the surface and ultimately detaches from the front as an eddy. The occurrence of essentially all cabbeling mass transformation near the surface is in contrast to the linear theory of Thomas and Shakespeare (2015) where mass transformation occurred at each vertical level via direct horizontal mixing. This difference means that mode water forming in the simulations is well mixed since the source water is a combination of water mass from multiple depths.

The linear theory of Thomas and Shakespeare (2015) predicts that the depth of maximum mode water formation via cabbeling is where the stratification associated with the cabbeled density profile [(14)] is minimized. Owing to the vertical exchange of water described above, here we argue that the density of the mode water is the average of the cabbeled density profile between this depth and the surface. Similarly, the temperature of the mode water is the average of the northern and southern profiles between this depth and the surface. We showed that this methodology for calculating the mode water properties is robust for a variety of northern and southern temperature–depth profiles, at least for a fully compensated front.

We have made a number of simplifications and assumptions in configuring the present model. The imposed background strain field is highly idealized compared to the strain fields associated with gyres or mesoscale eddies in the ocean. However, these real phenomena would have the same effect on the thermohaline front—that is, sharpening the front, thereby promoting instability and continually fluxing water mass in toward the front—albeit in a far more temporally and spatially variable fashion.

In addition, we have assumed that cabbeling is the dominant nonlinearity in the equation of state and that thermobaricity is by comparison negligible. We can test this assumption a posteriori using the model output. Thermobaricity results in a modification to the density $-\rho_0(\partial_P\alpha_T)\delta T\delta P$ given a change in pressure δP when combined with a change in temperature δT. For the temperatures and salinity values used in our simulations, the variation in thermal expansion coefficient with pressure $\partial_P\alpha_T$ is $\sim 2 \times 10^{-8}\,\mathrm{K}^{-1}\,\mathrm{dbar}^{-1}$. In the simulations, fluid parcels experience vertical displacements and hence pressure changes of order 100 dbar (e.g., Fig. 8), which if combined with $\sim 5°$ C temperature change for a fluid parcel mixed in the front, would yield a thermobaric density change of $0.01\,\mathrm{kg\,m^{-3}}$. This value is an order of magnitude weaker than the $0.1\,\mathrm{kg\,m^{-3}}$ density increase caused by cabbeling, indicating that neglecting thermobaric effects in our simulations was justified.

A further major assumption in our model is that of a fully compensated thermohaline front and the corresponding use of an artificially large cross-frontal temperature difference (10°C) and weak stratification to ensure the front becomes unstable. More realistic partially compensated fronts are unstable and have large turbulent mixing, which could enhance mode water formation. However, the fronts have much smaller cross-frontal temperature difference and stronger stratification, which could substantially reduce the resultant water mass transformation as per the scaling [(18)]. Further, it is unclear how the frontogenetic circulation at a noncompensated density front would modify the generation rate or T–S properties of the mode water. The thermally direct ageostrophic circulation associated with frontogenesis (e.g., Hoskins et al. 1978) would tend to preferentially bring water to the surface on the lower-density—typically the warmer, equatorward—side of the front, and this could significantly bias mode water properties toward the T–S properties of the warmer water. The thermally direct circulation could also lead to a preferential accumulation of the mode water at depth on the lighter side of the front, since it is associated with a flow at the base of the front from the denser to the lighter side.

In contrast to the front used in this study, the fronts where mode waters are observed have bounding water masses with properties that are maintained by sources and sinks of heat and salt on the large scale. Therefore, while mode water formation in our simulations is a transient process where formation terminates after the two distinct northern and southern water masses are mixed across the whole domain, at observed fronts it could be sustained. In addition, our model does not include any surface buoyancy fluxes, which are known to contribute significantly to mode water formation (Speer and Forget 2013). We anticipate that surface buoyancy loss will enhance the mass transformation via cabbeling by promoting the vertical exchange of fluid and bringing more water mass to the surface, but the water mass properties may be different to those predicted from cabbeling alone, particularly if the seasonality of the fluxes is considered. Conversely, the properties of the mode water formed would be different to those predicted by buoyancy fluxes alone since lateral mixing and cabbeling would be involved. Evidence to this effect is found in wintertime observations of Eighteen Degree

Water formed near the Gulf Stream. Here, Joyce et al. (2013) determined that the temperature and salinity of the mode water could not be explained solely by air–sea fluxes but required lateral mixing of cool freshwater from the north across the front.

Collectively, these processes found at observed fronts will give rise to a complicated steady-state mode water formation, which is likely to be different from the transient version seen in the present simulations. We will investigate these processes in a future work. Nevertheless, it is likely the cabbeling mechanism described here will still play an important role in determining the properties of the mode water.

Acknowledgments. L. N. T. was supported by NSF Grant OCE-1459677. C. J. S. acknowledges funding from the ARC Centre of Excellence for Climate System Science Grant Number CE1101028.

REFERENCES

Bishop, C. H., 1993: On the behaviour of baroclinic waves undergoing horizontal deformation. II: Error-bound amplification and Rossby wave diagnostics. *Quart. J. Roy. Meteor. Soc.*, **119**, 241–267, doi:10.1002/qj.49711951003.

Foster, T. D., 1972: An analysis of the cabbeling instability in sea water. *J. Phys. Oceanogr.*, **2**, 294–301, doi:10.1175/1520-0485(1972)002<0294:AAOTCI>2.0.CO;2.

Groeskamp, S., R. P. Abernathey, and A. Klocker, 2016: Water mass transformation by cabbeling and thermobaricity. *Geophys. Res. Lett.*, **43**, 10 835–10 845, doi:10.1002/2016GL070860.

Hanawa, K., and L. D. Talley, 2001: Mode waters. *Ocean Circulation and Climate: Observing and Modelling the Global Ocean*, G. Siedler, J. Church, and J. Gould, Eds., International Geophysics Series, Vol. 103, Academic Press, 373–386.

Hoskins, B. J., I. Draghici, and H. C. Davies, 1978: A new look at the ω-equation. *Quart. J. Roy. Meteor. Soc.*, **104**, 31–38, doi:10.1002/qj.49710443903.

Joyce, T. M., L. N. Thomas, W. K. Dewar, and J. B. Girton, 2013: Eighteen Degree Water formation within the Gulf Stream during CLIMODE. *Deep-Sea Res. II*, **91**, 1–10, doi:10.1016/j.dsr2.2013.02.019.

Klocker, A., and T. J. McDougall, 2010: Influence of the nonlinear equation of state on global estimates of dianeutral advection and diffusion. *J. Phys. Oceanogr.*, **40**, 1690–1709, doi:10.1175/2010JPO4303.1.

Lo Monaco, C., and N. Metzl, 2007: Marion Dufresne 35MF19980121 (OISO-01) cruise data from the 1998 cruises, CARINA data set. Carbon Dioxide Information Analysis Center, Oak Ridge National Laboratory, U.S. Department of Energy, accessed 16 November 2016, doi:10.3334/CDIAC/otg.CARINA_35MF19980121.

Marshall, J., A. Adcroft, C. Hill, L. Perelman, and C. Heisey, 1997: A finite-volume, incompressible Navier Stokes model for studies of the ocean on parallel computers. *J. Geophys. Res.*, **102**, 5753–5766, doi:10.1029/96JC02775.

——, and Coauthors, 2009: The Climode field campaign: Observing the cycle of convection and restratification over the Gulf Stream. *Bull. Amer. Meteor. Soc.*, **90**, 1337–1350, doi:10.1175/2009BAMS2706.1.

McDougall, T. J., 1987: Thermobaricity, cabbeling, and water-mass conversion. *J. Geophys. Res.*, **92**, 5448–5464, doi:10.1029/JC092iC05p05448.

Spall, M. A., 1997: Baroclinic jets in confluent flow. *J. Phys. Oceanogr.*, **27**, 1054–1071, doi:10.1175/1520-0485(1997)027<1054:BJICF>2.0.CO;2.

Speer, K., and G. Forget, 2013: Global distribution and formation of mode waters. *Ocean Circulation and Climate: A 21st Century Perspective*, 2nd ed. G. Siedler et al., Eds., International Geophysics Series, Vol. 103, Academic Press, 211–226.

Stone, P. H., 1970: On the non-geostrophic baroclinic instability: Part II. *J. Atmos. Sci.*, **27**, 721–726, doi:10.1175/1520-0469(1970)027<0721:ONGBSP>2.0.CO;2.

Talley, L. D., and J.-Y. Yun, 2001: The role of cabbeling and double diffusion in setting the density of the North Pacific Intermediate Water salinity minimum. *J. Phys. Oceanogr.*, **31**, 1538–1549, doi:10.1175/1520-0485(2001)031<1538:TROCAD>2.0.CO;2.

Thomas, L. N., and C. J. Shakespeare, 2015: A new mechanism for mode water formation involving cabbeling and frontogenetic strain at thermohaline fronts. *J. Phys. Oceanogr.*, **45**, 2444–2458, doi:10.1175/JPO-D-15-0007.1.

Urakawa, L., and H. Hasumi, 2012: Eddy-resolving model estimate of the cabbeling effect on the water mass transformation in the Southern Ocean. *J. Phys. Oceanogr.*, **42**, 1288–1302, doi:10.1175/JPO-D-11-0173.1.

Warren, B. A., 1972: Insensitivity of subtropical mode water characteristics to meteorological fluctuations. *Deep-Sea Res. Oceanogr. Abstr.*, **19**, 1–19, doi:10.1016/0011-7471(72)90069-1.

Winters, K. B., P. N. Lombard, J. J. Riley, and E. A. D'Asaro, 1995: Available potential energy and mixing in density-stratified fluids. *J. Fluid Mech.*, **289**, 115–128, doi:10.1017/S002211209500125X.

Worthington, L. V., 1959: The 18° water in the Sargasso Sea. *Deep-Sea Res.*, **5**, 297–305, doi:10.1016/0146-6313(58)90026-1.